A Potential-Theoretic Method for Far-Field Sound Radiation Calculations

S. I. Hariharan,*,1 J. R. Scott,† and K. L. Kreider*

*Department of Mathematics and Computer Science, The University of Akron, Akron, Ohio 44325-4002;
and †NASA Glenn Research Center at Lewis Field, Cleveland, Ohio 44135-3191

The far-field acoustic radiation due to the interaction of upstream, unsteady vortical disturbances with an airfoil in subsonic, compressible flow is calculated using potential theory. A Kirchhoff surface is placed in the near field surrounding the airfoil and the pressure on this surface is calculated from the unsteady flow field, obtained using a second-order finite-difference code. The governing equation is reduced to the Helmholtz equation in the frequency domain and the solution is written in terms of an integral over the Kirchhoff surface involving the free-space Green's function and an unknown single-layer density function. The single-layer density is then determined from the boundary condition on the Kirchhoff surface. This method is presented as an alternative to classical Kirchhoff methods. It has the advantage of being able to accommodate arbitrarily shaped Kirchhoff surfaces and is also readily extendable to three-dimensional problems. Numerical results are presented for thin, symmetric, and loaded airfoils. Thin-airfoil results are compared to the analytical solution, and thick-airfoil results are checked for numerical convergence and compared to results obtained from a time-domain Euler solver. © 2000 Academic Press

Key Words: compressible flows; aeroacoustics; singular integral equations; far-field calculations.

1. INTRODUCTION

The prediction of far-field sound radiation is a key area of interest in the computational aeroacoustics community. This subject is a common intersection for most unsteady external aerodynamic problems such as the gust response of airfoils, flutter problems, and jet noise. Since these problems are generally posed in open domains, it is difficult to extend the computational domains to the far field owing to the prohibitive cost of the computations involved. While state-of-the-art computers provide high speed and large storage capacity,

the numerical algorithms themselves are known to have problems—they are subject to dissipation and dispersion errors resulting from the disparity in magnitude between the (small) acoustic pressure and the dominant flow pressure, and these may contaminate acoustic calculations. In addition, the lack of analytical solutions for most problems of interest serves to hinder the development of numerical methods.

Current efforts involving the direct numerical simulation of far-field sound have been made by Tam [24], Tam and Webb [25], Hixon *et al.* [10, 11], Botteldooren [5], Fung *et al.* [8], Mitchell *et al.* [16], Djambazov *et al.* [6], Freund [7], Meadows and Atkins [15], Lyrintzis and co-workers [13, 14], and Stenger [21]. In addition, there is a sequence of numerical works by Atassi and his associates [2–4, 17, 18, 22, 23] dealing with frequency-domain problems. A summary of these efforts is found in [1]. These methods employ the numerical simulation of the near field, developed by Scott [19] and Scott and Atassi [20], and the construction of a Kirchhoff surface for the prediction of far-field sound using the Green's function technique.

In most of these works, the driving philosophy is the accurate numerical simulation of the near field and a "semi-analytical" approach to predicting the far-field sound. For example, the work of Atassi, and co-workers [2, 3, 17, 18, 22, 23] uses a Kirchhoff method and a modified Green's function approach wherein Kirchhoff's formula is used to predict the far-field sound. This method relies on constructing a specific Green's function for a circular Kirchhoff surface and requires the normal derivative of the pressure on the surface; a modified Green's function is then introduced to eliminate this need. The Green's function is expressed as an infinite series of higher order Hankel functions. Because the natural grid for the near-field pressure calculation is in elliptic coordinates, the pressure on the Kirchhoff circle must be interpolated and then numerically differentiated. Also, the series representation for the Green's function must be truncated.

This paper is motivated by a similar philosophy, but the key difference is in the formulation of the far-field sound radiation calculations. The method presented here, based on potential theory, has two specific goals: (i) to simplify the computation of the Green's function and (ii) to allow a convex arbitrary shape for the Kirchhoff surface. The potential theoretic approach presented here satisfies both goals. It requires only the free-space Green's function, which is simple to compute, and an unknown single-layer density. This single-layer density is determined by a technique proposed by Hariharan and MacCamy [9] for electromagnetic scattering problems. In addition, the Kirchhoff surface can be almost any shape, so long as the surface can be written in polar form ($r = f(\theta)$). This is attractive for studying jet noise problems, where the computational domains are often elongated. Finally, the method is extendable to three-dimensional geometries with little difficulty.

The Green's function representation of the far field, expressed in Eq. (41) below, is based on the single-layer potential. The choice of this as opposed to the double-layer potential is dictated mainly by convenience. The numerical procedure based on this formulation was verified with exact as well as semi-analytical solutions, and no conditioning problems were encountered. The implementation of a double-layer potential representation, which requires the normal derivative of the free-space Green function, is currently in progress, in order to do a quantitative comparison of the two formulations.

The application of the potential method to determining the far-field acoustics of an airfoil subjected to an upstream harmonic gust is shown here in detail. The calculations presented here for a thin airfoil are compared to an analytical solution, and thick-airfoil results are compared to a high-order time-domain Euler solver [10]. The near-field calculations are

performed by a second-order finite-difference code, GUST3D, developed by Scott [19] and Scott and Atassi [20].

2. PROBLEM FORMULATION

2.1. *Near-Field Formulation*

Consider inviscid, subsonic, compressible flow where the fluid is an ideal, non-heat-conducting gas with constant specific heat. Assume that there are no shocks, imposed entropy disturbances, or incident acoustic waves present. The time-dependent governing continuity and momentum equations are

$$\rho_t + \nabla \cdot (\rho \mathbf{U}) = 0 \tag{1}$$

$$\mathbf{U}_t + (\mathbf{U} \cdot \nabla)\mathbf{U} + \frac{1}{\rho}\nabla p = 0, \tag{2}$$

where ρ is density, p is pressure, and $\mathbf{U}$ is the fluid velocity. Place an arbitrary airfoil in the fluid so that the center of the three-dimensional coordinate system is at the center of the airfoil with the x_1 coordinate parallel to the upstream mean flow $U_\infty \mathbf{i}$. Assume that the upstream rotational part of the flow is small and that the mean flow is two dimensional. Then (1) and (2) are linearized about the mean flow using

$$\mathbf{U} = \mathbf{U}_0 + \mathbf{u} \tag{3}$$

$$\rho = \rho_0 + \rho' \tag{4}$$

$$p = p_0 + p', \tag{5}$$

where 0 subscripts indicate mean flow quantities and $'$ superscripts indicate time-dependent perturbation quantities. The upstream flow is given by

$$\mathbf{U}_\infty(\mathbf{x}, t) = U_\infty \mathbf{i} + \mathbf{u}_\infty(\mathbf{x} - iU_\infty t), \tag{6}$$

where $\mathbf{u}_\infty$ represents the imposed upstream rotational disturbance. Since the problem is linear, $\mathbf{u}_\infty$ can be decomposed into its Fourier components without loss of generality so that incident vortical gusts of the form

$$\mathbf{u}_\infty = \mathbf{a} \exp(i\mathbf{k} \cdot (\mathbf{x} - iU_\infty t)) \tag{7}$$

can be considered. In (7), $\mathbf{a}$ and $\mathbf{k}$ are the amplitude and wave number vectors of the disturbance, respectively, with $|\mathbf{a}| \ll U_\infty$. In addition, the continuity equation requires that $\mathbf{a} \cdot \mathbf{k} = 0$.

Substituting (3)–(5) into (1) and (2), and neglecting higher order terms, gives the linearized continuity and momentum equations

$$\frac{D_0\rho'}{Dt} + \rho'\nabla \cdot \mathbf{U}_0 + \nabla \cdot (\rho_0\mathbf{u}) = 0 \tag{8}$$

$$\rho_0\left(\frac{D_0\mathbf{u}}{Dt} + \mathbf{u} \cdot \nabla\mathbf{U}_0\right) + \rho'\mathbf{U}_0 \cdot \nabla\mathbf{U}_0 = -\nabla p', \tag{9}$$

where $D_0/Dt = \partial/\partial t + \mathbf{U}_0 \cdot \nabla$ is the convective derivative associated with the mean flow.

The unsteady velocity can be written as the sum of a known vortical component $\mathbf{u}^{(R)}$ (see [1]) and an unknown potential component as

$$\mathbf{u}(\mathbf{x}, t) = \mathbf{u}^{(R)} + \nabla\phi. \tag{10}$$

The unsteady potential ϕ satisfies the non-constant-coefficient convective wave equation given by

$$\frac{D_0}{Dt}\left(\frac{1}{c_0^2}\frac{D_0\phi}{Dt}\right) - \frac{1}{\rho_0}\nabla \cdot (\rho_0\nabla\phi) = \frac{1}{\rho_0}\nabla \cdot \left(\rho_0\mathbf{u}^{(R)}\right), \tag{11}$$

where c_0 is the mean flow speed of sound. The boundary conditions on ϕ are given by

$$\nabla\phi \cdot \mathbf{n} = 0 \qquad \text{(airfoil surface)} \tag{12}$$

$$\frac{D_0}{Dt}(\Delta\phi) = 0 \qquad \text{(wake)} \tag{13}$$

$$\Delta(\nabla\phi \cdot \mathbf{n}) = 0 \qquad \text{(wake)} \tag{14}$$

$$\nabla\phi \to -\nabla\tilde{\phi} \qquad \text{as } x_1 \to -\infty. \tag{15}$$

Equations (13) and (14) impose continuity of the pressure and normal velocity, respectively, across the wake, while (15) ensures that $\mathbf{u} \to \mathbf{u}_\infty$ as $x_1 \to -\infty$. $\tilde{\phi}$ is a known function of the upstream disturbance. For a complete discussion of the development of this boundary value problem, see [19, 20].

The unsteady pressure is related to ϕ through the equation

$$p' = -\rho_0(\mathbf{x})\frac{D_0\phi}{Dt}. \tag{16}$$

By determining ϕ, the acoustic pressure p' may then be calculated.

After nondimensionalizing appropriately, the boundary-value problem is simplified by applying the transformation

$$\phi = \psi \exp(-ik_1 t + ik_3 x_3 - iK_1\Phi_0), \tag{17}$$

where

$$K_1 = \frac{k_1 M_\infty^2}{\beta_\infty^2} \tag{18}$$

$$\beta_\infty = \sqrt{1 - M_\infty^2}. \tag{19}$$

M_∞ is the free-stream Mach number and Φ_0 is the mean flow potential function. The normalized wave number k_1 is called the reduced frequency and is given by

$$k_1 = \frac{\omega c}{2U_\infty}, \tag{20}$$

where c is the airfoil chord length and ω is the dimensional angular frequency. The transformation (17) converts the problem to the frequency domain and eliminates the spanwise coordinate x_3, allowing the calculation to be done in two dimensions.

The unsteady pressure in terms of the transformed potential is

$$p' = -\rho_0\left(-ik_1 + U_0^2\frac{\partial}{\partial\Phi_0}\right)\psi\exp(-ik_1t + ik_3x_3 - iK_1\Phi_0). \tag{21}$$

A function $\bar{p}$ is introduced such that

$$p' = \bar{p}\exp(-ik_1t + ik_3x_3 - iK_1\Phi_0) \tag{22}$$

with

$$\bar{p} = -\rho_0\left[-i\left(k_1 + U_0^2K_1\right)\psi + U_0^2\frac{\partial\psi}{\partial\Phi_0}\right]. \tag{23}$$

The unknown potential ψ and its derivative $\partial\psi/\partial\Phi_0$ are computed numerically [19, 20]. The calculation, which is quite involved, is part of the near-field computation, so details are omitted here. Equation (23) is used to obtain the pressure required for the boundary condition in the far-field formulation described below.

2.2. Far-Field Formulation

A Kirchhoff surface, denoted by Γ, is introduced to surround the airfoil in the near field, as shown in Fig. 1. The region exterior to Γ is denoted by Ω. The only assumptions are that Γ is smooth and that Γ is far enough away from the airfoil so that the mean flow quantities
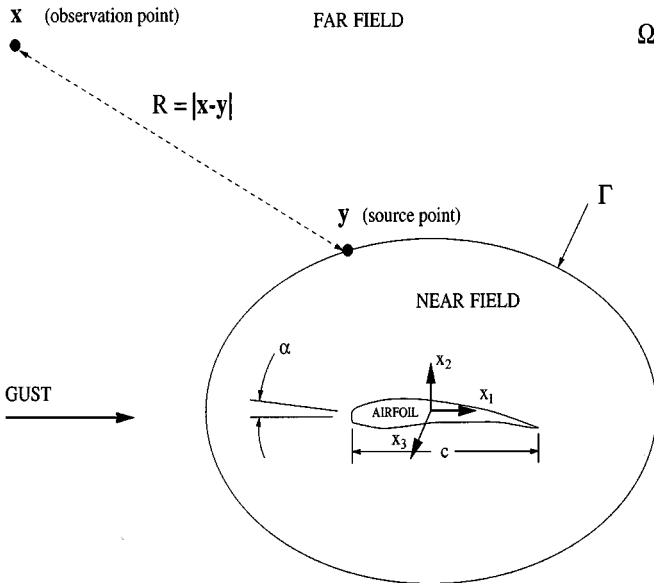
FIG. 1. Problem configuration. A periodic gust strikes an airfoil, and the far-field acoustic pressure is computed.

in Ω differ only slightly from those of the free stream. This allows the linearization of the continuity (1) and momentum (2) equations about the uniform mean flow using

$$\mathbf{U} = \mathbf{U}_\infty + \mathbf{u} \tag{24}$$

$$\rho = \rho_\infty + \rho' \tag{25}$$

$$p = p_\infty + p', \tag{26}$$

where ∞ subscripts indicate free-stream quantities. Substituting (24)–(26) into (1) and (2) gives the linearized continuity and momentum equations in Ω,

$$\frac{D_\infty \rho'}{Dt} + \rho_\infty \nabla \cdot \mathbf{u} = 0 \tag{27}$$

$$\rho_\infty \frac{D_\infty \mathbf{u}}{Dt} + \nabla p' = 0, \tag{28}$$

where $D_\infty/Dt = \partial/\partial t + U_\infty \partial/\partial x_1$. Applying the operators D_∞/Dt to (27) and ∇ to (28) gives

$$\frac{D_\infty^2 \rho'}{Dt^2} + \rho_\infty \frac{D_\infty}{Dt}(\nabla \cdot \mathbf{u}) = 0 \tag{29}$$

$$\rho_\infty \frac{D_\infty}{Dt}(\nabla \cdot \mathbf{u}) + \nabla^2 p' = 0. \tag{30}$$

To eliminate $\mathbf{u}$ from these equations, subtract (30) from (29) to obtain

$$\frac{D_\infty^2 \rho'}{Dt^2} = \nabla^2 p'. \tag{31}$$

Under the assumption of isentropic flow, the state equations relating p and ρ are

$$p = A\rho^\gamma, \quad \frac{\partial p}{\partial \rho} = c_\infty^2 \quad (\gamma = 1.4 \text{ for standard air}), \tag{32}$$

where A is a constant. Combining these with the linearizations in (25) and (26) gives the relation

$$p' = c_\infty^2 \rho'. \tag{33}$$

Substituting (33) into (31) gives

$$\frac{1}{c_\infty^2} \frac{D_\infty^2 p'}{Dt^2} = \nabla^2 p', \tag{34}$$

which reduces the problem to one dependent variable only, namely p'. Nondimensionalizing appropriately then gives the result

$$M_\infty^2 \left(\frac{\partial}{\partial t} + \frac{\partial}{\partial x_1}\right)^2 p' = \nabla^2 p'. \tag{35}$$

From this point, all quantities are assumed to be nondimensional.

Transforming the problem to the frequency domain using

$$p'(\mathbf{x}, t) = \bar{p}(x_1, x_2) \exp(-ik_1t + ik_3x_3 - iK_1x_1) \tag{36}$$

eliminates the dependence of the problem on time t and spanwise coordinate x_3. Since $\bar{p}$ approximates p from the near-field formulation equations (22) and (23), it is possible to calculate $\bar{p}$ numerically [19, 20] on Γ.

After an application of the transformation in (36), Eq. (35) becomes

$$\beta_\infty^2 \frac{\partial^2 \bar{p}}{\partial x_1^2} + \frac{\partial^2 \bar{p}}{\partial x_2^2} + \left(\frac{k_1^2 M_\infty^2}{\beta_\infty^2} - k_3^2 \right) \bar{p} = 0. \tag{37}$$

Finally, the coordinate system is transformed to the Prandtl–Glauert plane using the linear transformation

$$\begin{aligned} \tilde{x}_1 &= x_1 \\ \tilde{x}_2 &= \beta_\infty x_2. \end{aligned} \tag{38}$$

The transformed Kirchhoff surface is denoted by $\tilde{\Gamma}$ and the transformed domain by $\tilde{\Omega}$. Applying this transformation to Eq. (37) yields

$$\tilde{\nabla}^2 \bar{p} + K^2 \bar{p} = 0, \tag{39}$$

where

$$K^2 = \frac{k_1^2 M_\infty^2}{\beta_\infty^4} - \frac{k_3^2}{\beta_\infty^2}. \tag{40}$$

The problem has been reduced to a classical exterior problem governed by the Helmholtz equation, where the boundary conditions may be calculated numerically.

3. SOLUTION PROCEDURE

The solution procedure is based on single-layer potential theory [9]. There are two advantages to this formulation. First, the solution relies on a free-space Green's function rather than a specific Green's function that is dictated by the domain of the problem, making the numerical computation of the Green's function extremely simple. Second, arbitrarily shaped Kirchhoff surfaces may be used, whereas other methods may require a specified shape. This allows a great deal of flexibility in the numerical implementation, because the Kirchhoff surface may be adjusted to match any numerical grid used to determine the near-field pressure, which avoids interpolation of the pressure.

The solution to (39) may be expressed as

$$\bar{p}(\tilde{\mathbf{x}}) = \int_{\tilde{\Gamma}} \sigma(\tilde{\mathbf{y}}) G_f(\tilde{\mathbf{x}} \mid \tilde{\mathbf{y}}) \, ds_{\tilde{\mathbf{y}}}, \quad \tilde{\mathbf{x}} \in \tilde{\Omega}, \ \tilde{\mathbf{y}} \in \tilde{\Gamma}, \tag{41}$$

where σ is the density function, G_f is the free-space Green's function

$$G_f(\tilde{\mathbf{x}} \mid \tilde{\mathbf{y}}) = -\frac{i}{4} H_0^{(1)}(K|\tilde{\mathbf{x}} - \tilde{\mathbf{y}}|), \tag{42}$$

and $\bar{p}$ satisfies

- $\bar{p} \sim e^{iKR}/\sqrt{R}$ as $|\tilde{\mathbf{x}}| \to \infty$ with $R = |\tilde{\mathbf{x}} - \tilde{\mathbf{y}}|$
- $\bar{p} = \tilde{f}(\tilde{\mathbf{x}})$ on $\tilde{\Gamma}$.

As $\tilde{x}$ approaches the surface $\tilde{\Gamma}$, (41) becomes

$$\int_{\tilde{\Gamma}} \sigma(\tilde{\mathbf{y}}) G_f(\tilde{\mathbf{x}} \mid \tilde{\mathbf{y}}) \, ds_{\tilde{\mathbf{y}}} = \tilde{f}(\tilde{\mathbf{x}}), \quad \tilde{\mathbf{x}}, \tilde{\mathbf{y}} \in \tilde{\Gamma}. \tag{43}$$

This is a singular integral equation (with logarithmic singularity) of the first kind. The existence of solutions to this type of equation has been shown by several authors. Some of the earliest results were proposed by Hsiao and MacCamy [12]. A procedure for solving Eq. (43) for σ is outlined below. Upon calculating σ and substituting in (41), one can determine $\bar{p}$ at any point $\tilde{\mathbf{x}} \in \tilde{\Omega}$.

To allow an arbitrary shape of the Kirchhoff surface, assume that $\tilde{\Gamma}$ is polar-representable (can be expressed as a function $r = R(\theta)$). Let $\tilde{\mathbf{x}}$ and $\tilde{\mathbf{y}}$ (both on $\tilde{\Gamma}$) be expressed in polar coordinates as

$$\tilde{\mathbf{x}}(\theta) = (R(\theta) \cos \theta, R(\theta) \sin \theta) \tag{44}$$

$$\tilde{\mathbf{y}}(\phi) = (R(\phi) \cos \phi, R(\phi) \sin \phi), \tag{45}$$

and let

$$\tilde{f}(\tilde{\mathbf{x}}) \equiv \hat{f}(\theta), \quad \sigma(\tilde{\mathbf{y}}) \equiv \hat{\sigma}(\phi). \tag{46}$$

The distance between the two points $\tilde{\mathbf{x}}$ and $\tilde{\mathbf{y}}$ is then given by

$$|\tilde{\mathbf{x}} - \tilde{\mathbf{y}}| = \sqrt{R^2(\theta) + R^2(\phi) - 2R(\theta)R(\phi)\cos(\theta - \phi)}$$
$$\equiv d(\theta, \phi), \tag{47}$$

and the Green's function becomes

$$G_f(\tilde{\mathbf{x}} \mid \tilde{\mathbf{y}}) = -\frac{i}{4} H_0^{(1)}(K|\tilde{\mathbf{x}} - \tilde{\mathbf{y}}|)$$
$$= -\frac{i}{4} H_0^{(1)}(K \, d(\theta, \phi))$$
$$\equiv \hat{G}(\theta \mid \phi). \tag{48}$$

In terms of $d\phi$, ds is given by

$$ds = \sqrt{R'^2(\phi) + R^2(\phi)} \, d\phi. \tag{49}$$

Substituting these quantities into (43) yields

$$\hat{f}(\theta) = \int_0^{2\pi} \hat{\sigma}(\phi) \hat{G}(\theta \mid \phi) \sqrt{R'^2(\phi) + R^2(\phi)} \, d\phi, \quad \theta \in [0, 2\pi). \tag{50}$$

By defining $\bar{\sigma}(\phi) \equiv \sigma(\phi)\sqrt{R'^2 + R^2}$, the final equation is obtained:

$$\hat{f}(\theta) = \int_0^{2\pi} \bar{\sigma}(\phi) \hat{G}(\theta \mid \phi) \, d\phi, \quad \theta \in [0, 2\pi). \tag{51}$$

There is a logarithmic singularity in $\hat{G}$ (42) when $\theta = \phi$, which makes a direct numerical approximation of (51) impossible. The formulation must therefore be recast into a form that avoids numerical difficulties. To do this, first note that the zero-order Hankel function of the first kind may be expressed by

$$-\frac{i}{4}H_0^{(1)}(z) = \frac{1}{2\pi}\log(z) + \hat{\gamma} - \frac{i}{4} + \hat{T}(z), \tag{52}$$

where $\hat{\gamma} = (\gamma - \log 2)/2\pi$. Here, γ is Euler's constant and $\hat{T}(z) \to 0$ as $z \to 0$. This means that $\hat{G}$ may be written as

$$\hat{G}(\theta \mid \phi) = \frac{1}{2\pi}\log(K\,d(\theta,\phi)) + \hat{\gamma} - \frac{i}{4} + \hat{T}(K\,d(\theta,\phi)). \tag{53}$$

Next, observe that when $\theta \to \phi$, $R(\theta)$ can be expanded in a neighborhood of ϕ by a Taylor series. This allows $d(\theta,\phi)$ to be written in this limiting case as

$$d(\theta,\phi) = 2\sin\left(\frac{|\theta - \phi|}{2}\right)\sqrt{R'^2(\phi) + R^2(\phi)}. \tag{54}$$

This confines the singularity which arises in (53) to the factor $\log(\sin(|\theta - \phi|/2))$.

The next step is to rewrite (51) as

$$\hat{f}(\theta) = \int_0^{2\pi}(\bar{\sigma}(\phi) - \bar{\sigma}(\theta))\hat{G}(\theta \mid \phi)\,d\phi + \bar{\sigma}(\theta)\int_0^{2\pi}\hat{G}(\theta \mid \phi)\,d\phi, \quad \theta \in [0, 2\pi). \tag{55}$$

This formulation is preferable to (51) for two reasons. First, the first integral in (55) can be computed numerically without difficulty because the integrand can be shown to approach zero as $\theta \to \phi$. Second, the singularity in $\hat{G}$ in the second integral can be drawn out analytically, leaving an integral with a regular integrand, which can easily be computed numerically. Specifically, substituting (53) and (54) into $\hat{G}$ yields the expression for the second integral, for $\theta \in [0, 2\pi)$,

$$\int_0^{2\pi}\hat{G}(\theta \mid \phi)\,d\phi = \int_0^{2\pi}\left[\frac{1}{2\pi}\log(Q) + \hat{\gamma} - \frac{i}{4} + \hat{T}(\theta,\phi)\right]d\phi$$

$$= \int_0^{2\pi}\frac{1}{2\pi}\left[\log\left(\sin\left(\frac{|\theta - \phi|}{2}\right)\right) + \bar{T}(\theta,\phi)\right]d\phi, \tag{56}$$

where $\bar{T}$ and Q are defined by

$$\bar{T} = \begin{cases} \hat{\gamma} - \frac{i}{4} + \frac{1}{2\pi}\log(2K\sqrt{R'^2(\phi) + R^2(\phi)}), & \theta = \phi \\ -\frac{i}{4}H_0^{(1)}(K\,d(\theta,\phi)) - \frac{1}{2\pi}\log\left(\sin\left[\frac{|\theta-\phi|}{2}\right]\right), & \theta \neq \phi \end{cases} \tag{57}$$

$$Q = 2K\sqrt{R'^2(\phi) + R^2(\phi)}\sin\left(\frac{|\theta - \phi|}{2}\right). \tag{58}$$

It is important to note that $\bar{T}$ is regular and that the singularity appears only in the first term on the right in (56). Using complex analysis, one can obtain the exact value of this

integral, namely

$$\frac{1}{2\pi} \int_0^{2\pi} \log\left(\sin\left(\frac{|\theta - \phi|}{2}\right)\right) d\phi = -\log(2). \tag{59}$$

Substituting this result into (55) gives

$$\hat{f}(\theta) = \int_0^{2\pi} (\bar{\sigma}(\phi) - \bar{\sigma}(\theta))\hat{G}(\theta \mid \phi) \, d\phi - \bar{\sigma}(\theta)\log(2) + \bar{\sigma}(\theta) \int_0^{2\pi} \bar{T}(\theta, \phi) \, d\phi,$$
$$\theta \in [0, 2\pi). \quad (60)$$

This equation can easily be solved numerically because the two integrands are regular. The numerical procedure for finding $\bar{\sigma}$ can now be developed.

4. NUMERICAL PROCEDURE

To determine the solution numerically, a suitable shape for the Kirchhoff surface must be specified. The choice of an ellipse is convenient, not only because analytical representations for $R(\theta)$ and $R'(\theta)$ are available, but also because it is most convenient to solve for the near-field pressure using elliptic coordinates, so that the Kirchhoff surface may be specified on a near-field gridline to avoid interpolation error in the pressure.

The goal is to solve (60) numerically for $\bar{\sigma}(\theta)$ so that it can be used in (41) to obtain $\bar{p}$ in the far field. The procedure is described in general here, and implementation issues are discussed in the next section.

A numerical representation of (60) can be obtained using rectangular quadrature. Choose a discretization constant n and let $h = 2\pi/n$. For $i, j = 1, \ldots, n$, define $\phi_j = (j - 1/2)h$ and $\theta_i = (i - 1/2)h$. Then, (60) becomes

$$\sum_{j=1}^{n} A_{ij}\bar{\sigma}_j = \hat{f}_i, \tag{61}$$

where $A_{ij} = A(\theta_i, \phi_j)$, $\bar{\sigma}_j = \bar{\sigma}(\phi_j)$, and $\hat{f}_i = \hat{f}(\theta_i)$. The near-field solver is used to determine the values of $\bar{p}$, and hence $\hat{f}_i$, at a finite number of points on the Kirchhoff surface. The A_{ij} values are given by

$$A_{ij} = \begin{cases} -\log(2) + \left[\sum_{k=1}^{n} \bar{T}_{ik}h - \sum_{k=1(k\neq i)}^{n} \hat{G}_{ik}h\right], & i = j \\ \hat{G}_{ij}h, & i \neq j \end{cases}, \tag{62}$$

where $\bar{T}_{ij} = \bar{T}(\theta_i, \phi_j)$ and $\hat{G}_{ij} = \hat{G}(\theta_i, \phi_j)$. An equation is obtained for each $i = 1, \ldots, n$, yielding an $n \times n$ linear system, which can be solved by any standard method for the unknowns $\bar{\sigma}_1, \ldots, \bar{\sigma}_n$.

Once $\{\bar{\sigma}_j\}$ is obtained, it is a rather simple matter to obtain $\bar{p}$ at any point $\mathbf{x} \in \Omega$. It is first necessary to transform the point to $\tilde{\mathbf{x}} \in \tilde{\Omega}$ using (38). Let $\tilde{\mathbf{x}}$ be represented as

$$\tilde{\mathbf{x}} = (r\cos\theta, r\sin\theta), \tag{63}$$

where r and θ are fixed, and let $\tilde{\mathbf{y}} \in \tilde{\Gamma}$ be defined as

$$\tilde{\mathbf{y}} = (R(\phi) \cos \phi, \, R(\phi) \sin \phi), \quad \phi \in [0, 2\pi). \tag{64}$$

Therefore, the distance between $\tilde{\mathbf{x}}$ and $\tilde{\mathbf{y}}$ is given by

$$\begin{aligned}
|\tilde{\mathbf{x}} - \tilde{\mathbf{y}}| &= \sqrt{[r \cos \theta - R(\phi) \cos \phi]^2 + [r \sin \theta - R(\phi) \sin \phi]^2} \\
&= \sqrt{r^2 + R^2(\phi) - 2r R(\phi) \cos(\theta - \phi)} \\
&= d(r, \theta, \phi),
\end{aligned} \tag{65}$$

and the Green's function becomes

$$\hat{G}(\theta, \phi) = -\frac{i}{4} H_0^{(1)}(K \, d(r, \theta, \phi)). \tag{66}$$

As follows from (41), the solution is

$$\bar{p}(r, \theta) = -\frac{i}{4} \int_0^{2\pi} \bar{\sigma}(\phi) H_0^{(1)}(K \, d(r, \theta, \phi)) \, d\phi. \tag{67}$$

This can be expressed numerically as

$$\bar{p}(r, \theta) = -\frac{i}{4} \sum_{j=1}^{n} \bar{\sigma}_j H_0^{(1)}(K \, d(r, \theta, \phi_j)) h. \tag{68}$$

5. RESULTS AND DISCUSSION

A number of numerical computations are presented here for thin, symmetric, and loaded airfoils for a variety of flows and gusts. Thin-airfoil results, which appear in Section 5.1, are compared with the analytical solution. Symmetric-airfoil results appear in Section 5.2. There is no analytical solution to compare with, so a convergence study is presented, as is a comparison with an Euler solver [10]. Loaded-airfoil results appear in Section 5.3; again, a convergence study is presented.

All calculations except those shown in Fig. 11 employ a circular Kirchhoff surface. The number of discretization points is 120 for a flat plate and 240 for a thick airfoil. The system of equations generated is solved using Gaussian elimination with pivoting.

The configuration of the gust is shown in Fig. 2. Polar directivity plots of the solution on a circle of radius R_{far} appear below. The solution is normalized by multiplying the acoustic pressure by $\sqrt{R_{\text{far}}}$ to remove its dependence on the far-field radius.

To interpret the directivity plots, note that $|p'| = |\bar{p}|$ since p' and $\bar{p}$ are related to each other through a complex exponential factor (Eq. (36)). For each observation point in the far field, the point

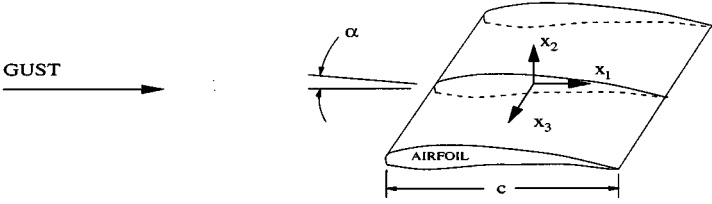$$\sqrt{R_{\text{far}}}(|p'| \cos \theta, \, |p'| \sin \theta)$$

is plotted, where θ is the polar angle of the observation point, as shown in Fig. 3. Lobes indicate directions of noise propagation, while the absence of lobes indicates a zone of silence.
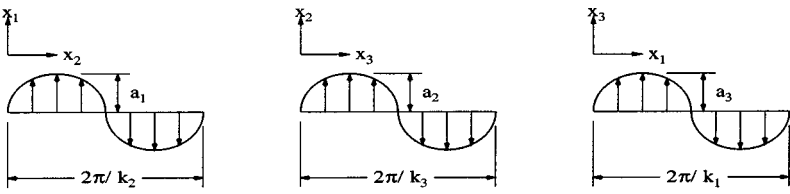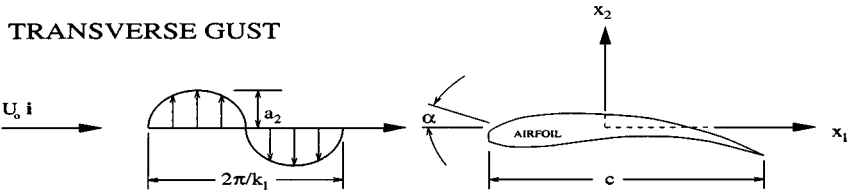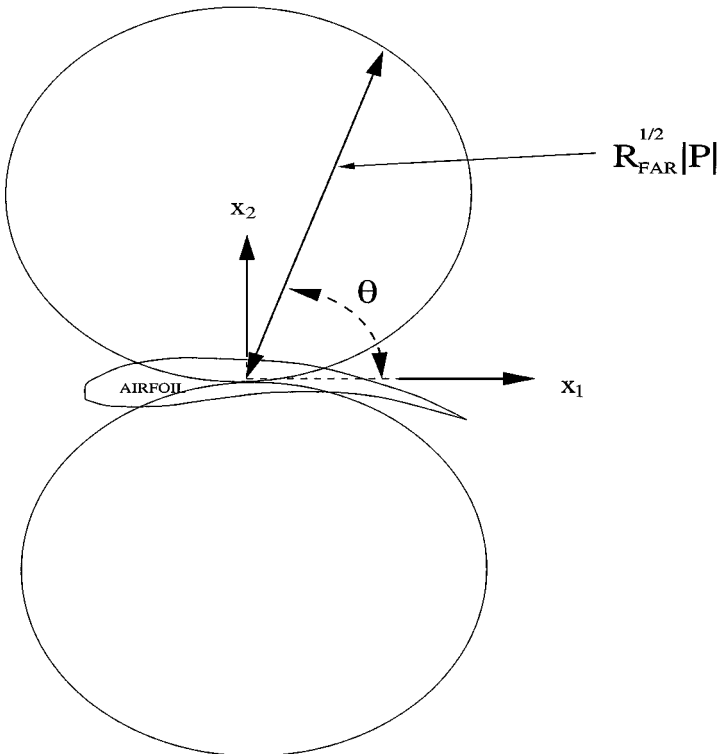
FIG. 2. Gust configuration. A transverse gust travels along the x_1 axis with amplitude a_2 along the x_2 axis. A longitudinal gust travels along the x_2 axis with amplitude a_1 along the x_1 axis. An oblique gust travels along the x_3 axis with amplitude a_2 along the x_2 axis.

FIG. 3. Polar directivity plot. At any given angle θ, a large radial amplitude indicates strong noise propagation, while a small radial amplitude indicates weak noise propagation.
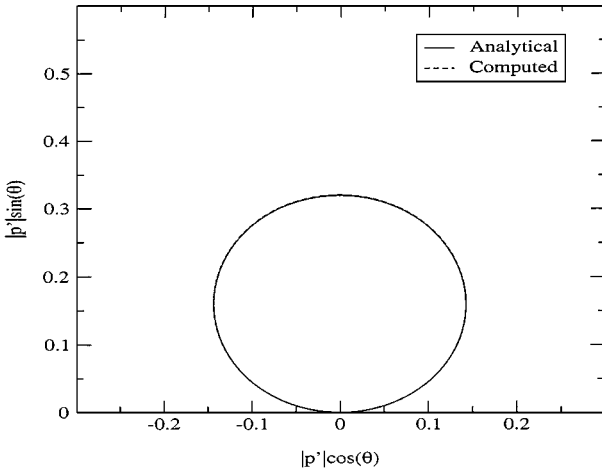
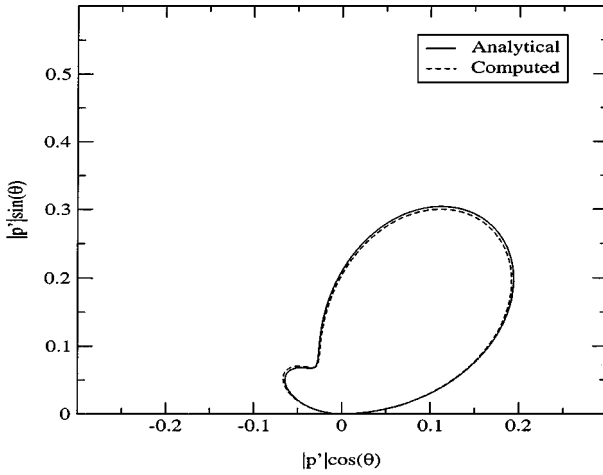**FIG. 4.** Comparison of computed and analytical far-field pressure for a flat plate at $M = 0.5$ and $k_1 = 0.1$.

5.1. *Thin-Airfoil Results*

The far-field pressure was computed for a thin airfoil in flows with Mach numbers $M = 0.5$ and 0.8 and reduced frequencies $k_1 = 0.1$, 1.0, and 3.0. A Kirchhoff circle of radius 2.0 (one chord length) was used. The near-field pressure was obtained by running GUST3D to numerical convergence, but no other attempt was made to optimize the results. Figures 4–9 show the comparison of the computed pressure with the analytical solution at a far-field radius of 100 for the various cases. The results are nearly perfect for the lower frequencies and degrade only slightly for the higher frequencies. The accuracy depends only slightly on the Mach number.

Analytically, these results should be independent of the radius of the Kirchhoff circle used, because the mean flow is not disrupted by the thin airfoil. However, there are slight differences in the numerical results, mainly caused by the approximate far-field boundary
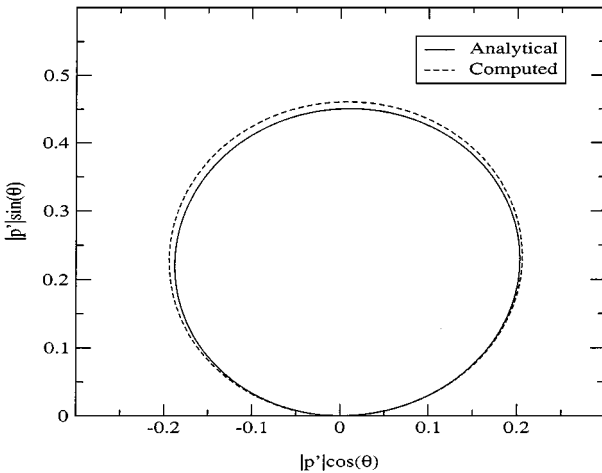
FIG. 5. Comparison of computed and analytical far-field pressure for a flat plate at $M = 0.5$ and $k_1 = 1.0$.

FIG. 6. Comparison of computed and analytical far-field pressure for a flat plate at $M = 0.5$ and $k_1 = 3.0$.
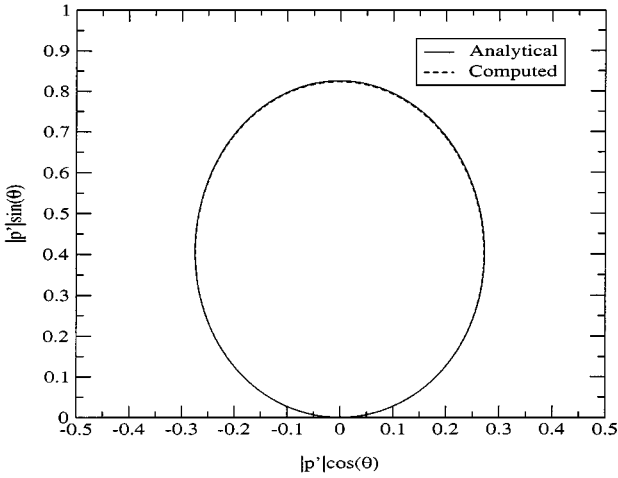

FIG. 7. Comparison of computed and analytical far-field pressure for a flat plate at $M = 0.8$ and $k_1 = 0.1$.
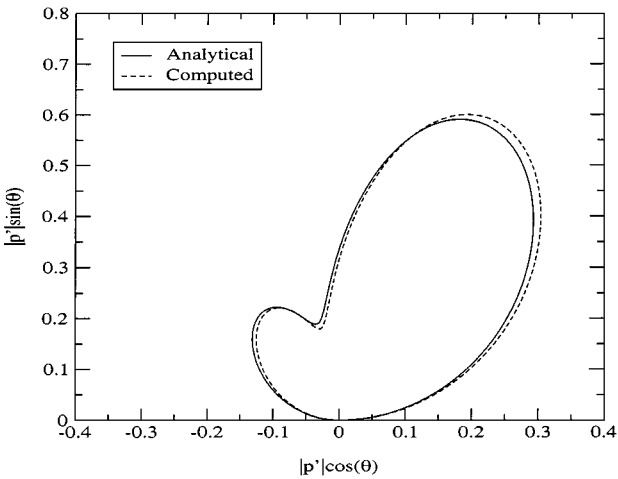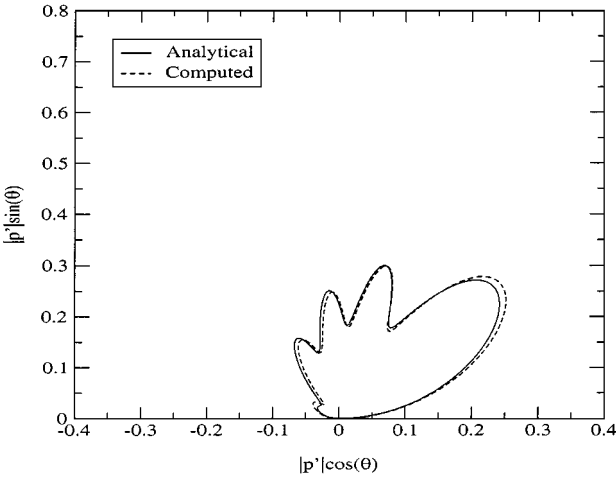

FIG. 8. Comparison of computed and analytical far-field pressure for a flat plate at $M = 0.8$ and $k_1 = 1.0$.

FIG. 9. Comparison of computed and analytical far-field pressure for a flat plate at $M = 0.8$ and $k_1 = 3.0$.

condition used in the near-field solver. Figure 10 shows these differences for an extreme case, $M = 0.8$, $k_1 = 3.0$ for Kirchhoff radii of 1.5, 2.0, and 2.5. Although the results are slightly inaccurate, the differences caused by changing the radius are not significant. For smaller values of M and k_1, the differences are even slighter.

The effect of changing the shape of the Kirchhoff surface can be seen in Fig. 11. Mach number $M = 0.8$ and reduced frequencies $k_1 = 0.1$, 1.0, and 3.0 were used with a circular Kirchhoff surface of radius 2 and an elliptical surface with $\xi = 0.45$, where $x = \cos(\pi\eta)\cosh(\pi\xi)$, $y = \sin(\pi\eta)\sinh(\pi\xi)$. The elliptical surface coincides with the near-field grid, so the pressure values are obtained without interpolation, whereas the circular surface requires interpolation of the pressure. The plots in Fig. 11 indicate that there is a minimal effect in changing the shape of the Kirchhoff surface.
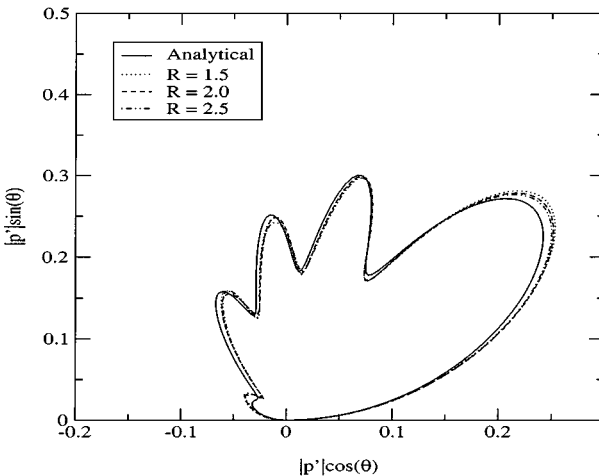
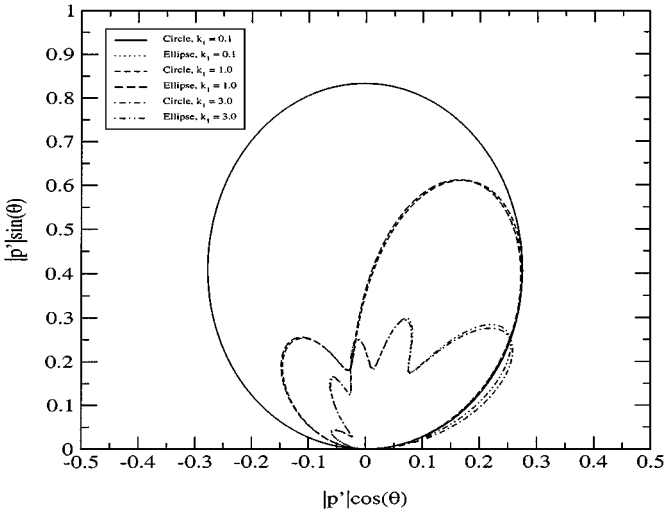**FIG. 10.** Effect of changing the Kirchhoff radius for a flat plate at $M = 0.8$ and $k_1 = 3.0$.

FIG. 11.   Circular and elliptical Kirchhoff surfaces for a flat plate at $M = 0.8$ and $k_1 = 0.1$, 1.0, and 3.0.

5.2. *Symmetric-Airfoil Results*

The far-field pressure was computed for a 12% thick unloaded Joukowski airfoil in flows with Mach number $M = 0.5$. Transverse gust results are shown in Fig. 12 (reduced frequency $k_1 = 0.1$) and Fig. 13 (reduced frequency $k_1 = 1.0$), and 2D gust (with transverse and longitudinal components) results are shown in Fig. 14 ($k_1 = k_2 = 0.1$) and Fig. 15 ($k_1 = k_2 = 1.0$). The intent in these cases is to gauge the effect of changing the location of the Kirchhoff surface. There are two competing considerations: (i) the surface must be far enough from the airfoil to be in the freestream region, so that the free-space Green's
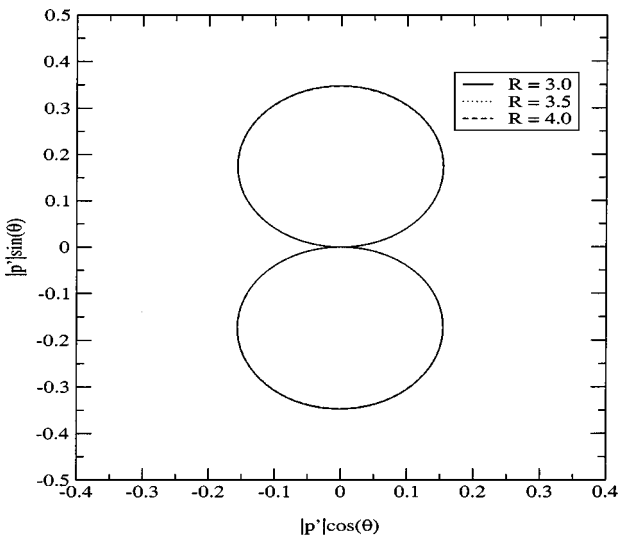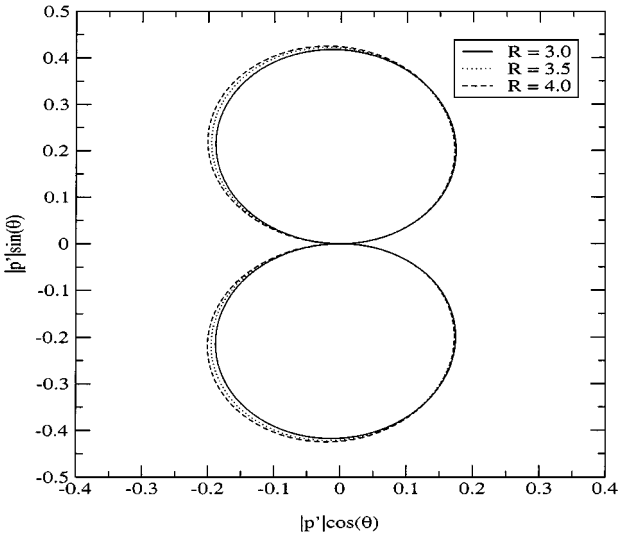

FIG. 12.   Far-field pressure for a 12% thick, unloaded Joukowski airfoil using three Kirchhoff radii, at $M = 0.5$, $k_1 = 0.1$, and $k_2 = 0.0$.
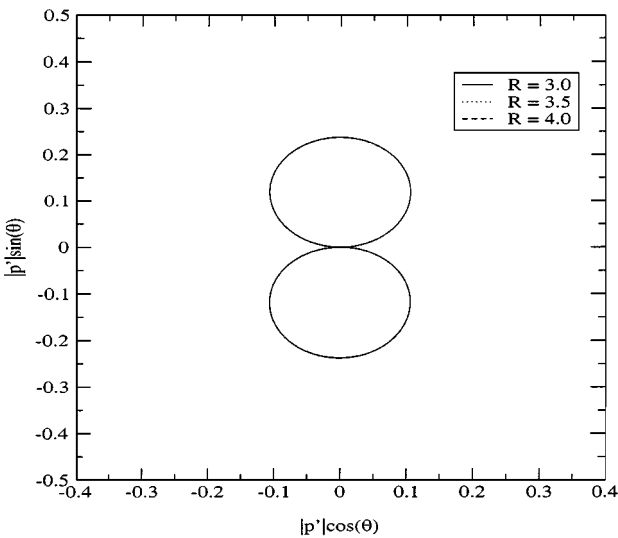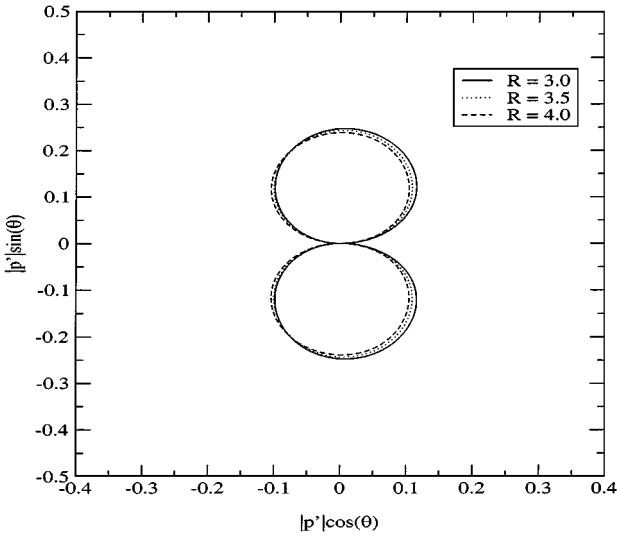
FIG. 13. Far-field pressure for a 12% thick, unloaded Joukowski airfoil using three Kirchhoff radii, at $M = 0.5$, $k_1 = 1.0$, and $k_2 = 0.0$.

function is valid, and (ii) the surface must be close enough to the airfoil for the near-field solver to provide accurate pressure values $\bar{\sigma}$ (the numerical grid used by the scheme is concentrated near the airfoil and so is more accurate there).

In the cases presented in Figs. 12–15, Kirchhoff radii of 3.0, 3.5, and 4.0 were used. For a radius of 3.0, the maximum deviation from mean flow is 0.87%. For a radius of 3.5, the maximum deviation from mean flow is 0.61%. For a radius of 4.0, the maximum deviation from mean flow is 0.45%. For the low-frequency cases (Figs. 12 and 14), changing the Kirchhoff radius has virtually no effect, so it may be surmised that the potential method has


FIG. 14. Far-field pressure for a 12% thick, unloaded Joukowski airfoil using three Kirchhoff radii, at $M = 0.5$, $k_1 = 0.1$, and $k_2 = 0.1$.

FIG. 15. Far-field pressure for a 12% thick, unloaded Joukowski airfoil using three Kirchhoff radii, at $M = 0.5$, $k_1 = 1.0$, and $k_2 = 1.0$.

converged numerically. The plots for the higher frequency cases (Figs. 13 and 15) do not show perfect agreement, but the results are well within the desired range of consistency.

There are no analytical solutions available for comparison, so the results above constitute only a check of numerical convergence. To help validate the method, a comparison with a time-domain Euler solver [10] (a prefactored sixth-order compact solver with optimized Runge–Kutta time stepping) was done for the same airfoil in a mean flow with Mach number $M = 0.5$ and transverse gusts with reduced frequencies $k_1 = 0.1, 1.0$. The corresponding acoustic intensities on a circle of radius 4 chord lengths (for a 2% magnitude gust) are shown in Figs. 16 and 17. The agreement between the results may be considered to be quite good, considering that they were obtained using completely different approaches. It should
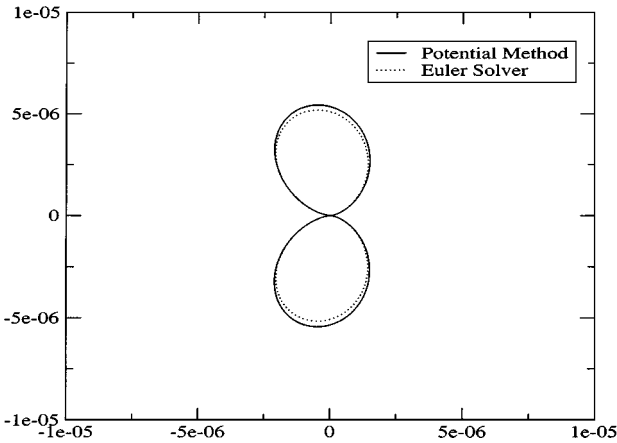
FIG. 16. Acoustic intensity on a circle of radius 4 chord lengths for a symmetric Joukowski airfoil, at $M = 0.5$, $k_1 = 0.1$, and $k_2 = 0.0$.
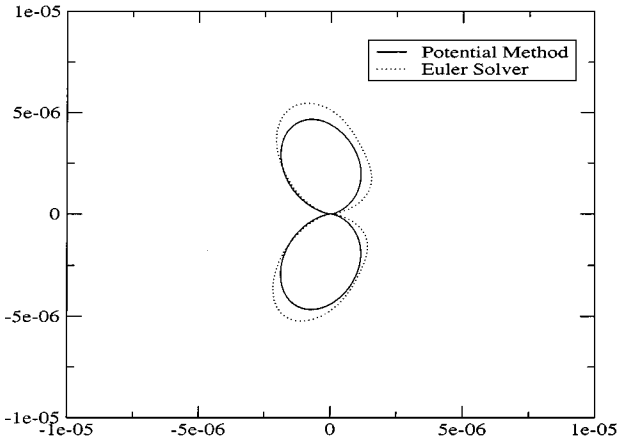
FIG. 17. Acoustic intensity on a circle of radius 4 chord lengths for a symmetric Joukowski airfoil, at $M = 0.5$, $k_1 = 1.0$, and $k_2 = 0.0$.

be noted that the Euler solver takes 72 h on a two-processor SGI Octane with R10000 chip, whereas the near-field solver and potential method combined takes less than 3 min on a Pentium II 400-MHz personal computer.

5.3. *Loaded-Airfoil Results*

The far-field pressure was computed for a 12% thick airfoil with an angle of attack of $2°$ and a camber ratio of 0.02 in flows with Mach number $M = 0.5$. Transverse gust results are shown in Fig. 18 (reduced frequency $k_1 = 0.1$) and Fig. 19 (reduced frequency $k_1 = 1.0$), and 2D gust results are shown in Fig. 20 ($k_1 = k_2 = 0.1$) and Fig. 21 ($k_1 = k_2 = 1.0$). A variety of Kirchhoff radii were used to gauge the influence of the deviation from mean flow. For a radius of 3.0, the maximum deviation from mean flow is 3.7%. For a radius of 3.5, the
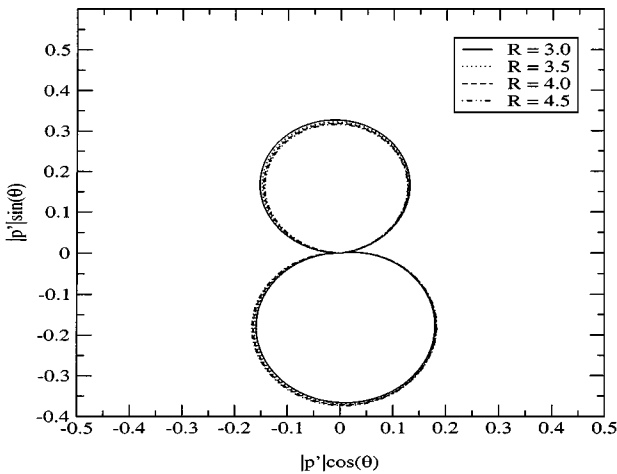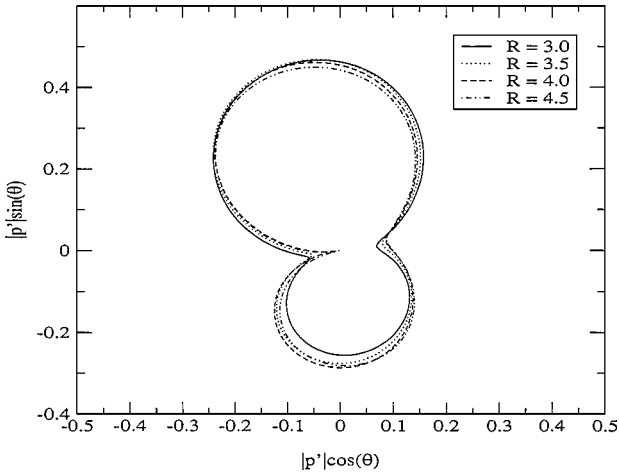

FIG. 18. Far-field pressure for a 12% thick, loaded Joukowski airfoil using four different Kirchhoff radii, at $M = 0.5$, $k_1 = 0.1$, and $k_2 = 0.0$.
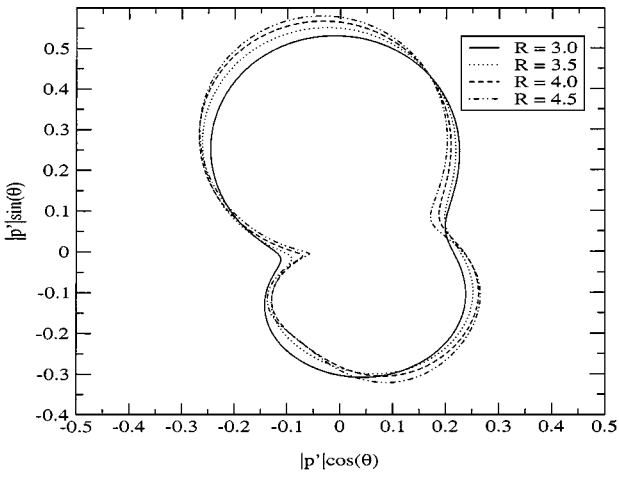
FIG. 19. Far-field pressure for a 12% thick, loaded Joukowski airfoil using four different Kirchhoff radii, at $M = 0.5$, $k_1 = 1.0$, and $k_2 = 0.0$.
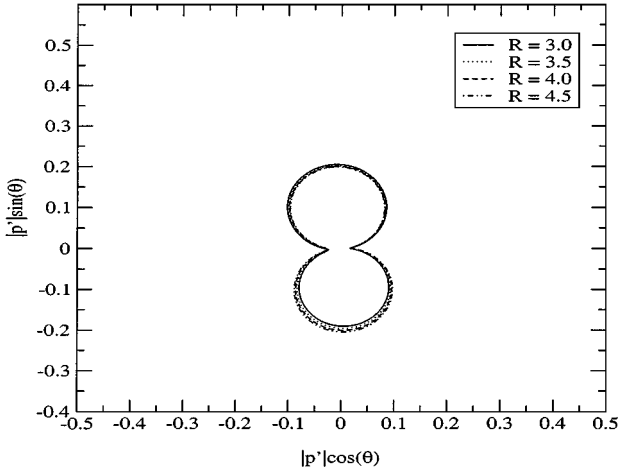
FIG. 20. Far-field pressure for a 12% thick, loaded Joukowski airfoil using four different Kirchhoff radii, at $M = 0.5$, $k_1 = 0.1$, and $k_2 = 0.1$.

FIG. 21. Far-field pressure for a 12% thick, loaded Joukowski airfoil using four different Kirchhoff radii, at $M = 0.5$, $k_1 = 1.0$, and $k_2 = 1.0$.

maximum deviation from mean flow is 3.1%. For a radius of 4.0, the maximum deviation from mean flow is 2.7%. For a radius of 4.5, the maximum deviation from mean flow is 2.4%. In the first case, $M = 0.5$, $k_1 = 0.1$, shown in Fig. 18, the results for radius 4.0 and 4.5 are nearly the same, indicating numerical convergence, but in the other cases, it is clear that a larger Kirchhoff radius is needed. Nevertheless, the degree of consistency here is acceptable.

6. CONCLUSION

The analytical development of the potential method for far-field acoustic radiation from airfoils is presented here, as is a description of its numerical implementation. This method has several features that make it attractive:

- The potential method is easy to implement, because (i) only simple standard numerical techniques are needed (rectangular quadrature, Gauss–Jordan elimination with pivoting, and possibly linear interpolation) and (ii) the potential method does not require the involved calculation of a problem-dependent Green's function but uses the well-known, easily computed free-space Green's function.
- The potential method is flexible in that the Kirchhoff surface is arbitrary and can be made to coincide with the near-field solver grid to avoid interpolation of the near-field pressure. Even so, the effect of interpolation is minimal.
- The potential method may be coupled with any near-field solver, as long as the near-field computational domain extends a reasonable distance into the free-stream region.
- The potential method is easily extended to completely three-dimensional problems.

The numerical results presented here demonstrate an accuracy of 10% or better, which is generally within an acceptable range of engineering accuracy. A substantial amount of validation has been done; this work indicates that for reduced frequencies k_1 up to about 1, far-field results are very good, and for reduced frequencies up to about 1.5, far-field results are acceptable. For higher reduced frequencies, an improved near-field solver must be developed before far-field results can be considered acceptable. However, the main question in this paper, *how well does the potential method propagate near-field acoustics to the far field?* has been clearly answered—the potential method provides accurate far-field pressure profiles. The method can be considered a viable alternative to existing approaches.

Future work includes the continuing parameter study of the method for the gust response of unloaded and loaded thick airfoils, the development of a more accurate near-field solver, and the extension of the method to three-dimensional acoustic problems involving sources more complicated than gusts.

REFERENCES

1. H. M. Atassi, Unsteady aerodynamics of vortical flows: Early and recent developments, in *Symposium on Aerodynamics and Aeroacoustics, Feb. 28–March 2, 1993*.

2. H. M. Atassi, S. Subramaniam, and J. R. Scott, *Acoustic Radiation from Lifting Airfoils in Compressible Subsonic Flows*, AIAA Paper 90-3911 (1990).

3. H. M. Atassi, M. Dusey, and C. M. Davis, *Acoustic Radiation from a Thin Airfoil in Nonuniform Subsonic Flows*, AIAA Paper 90-3910 (1990).

4. H. M. Atassi and J. Grzedzinski, Unsteady disturbances of streaming motions around bodies, *J. Fluid Mech.* **209**, 385 (1989).

5. D. Botteldooren, Vorticity and entropy boundary conditions for acoustical finite-difference time-domain simulations, *J. Acoust. Soc. Am.* **102**, 170 (1997).

6. G. Djambazov, C. H. Lai, and K. Pericleous, Development of numerical techniques for near field aeroacoustic computations, *Int. J. Numer. Meth. Fluids* **29**, 719 (1999).

7. J. B. Freund, A simple method for computing far-field sound in aeroacoustic computations, *J. Comput. Phys.* **157**, 796 (2000).

8. K. Y. Fung, S. Davis, and R. S. O. Man, Implicit high-order compact algorithm for computational acoustics, *AIAA J.* **34**, 2029 (1996).

9. S. I. Hariharan and R. C. MacCamy, Integral equation procedures for eddy current problems, *J. Comput. Phys.* **45**, 80 (1982).

10. R. Hixon, R. R. Mankbadi, and J. R. Scott, Application of a high-order finite-difference scheme to the airfoil–gust problem, prepared for the 2001 Aerospace Sciences Meeting, Reno NV, January 2001.

11. R. Hixon, S.-H. Shih, R. R. Mankbadi, and J. R. Scott, *Time Domain Solution of the Airfoil Gust Problem Using a High-Order Compact Scheme*, AIAA Paper 93-3241, presented at the Joint Propulsion Conference, July 13–15, 1998, Cleveland, OH.

12. G. C. Hsiao and R. C. MacCamy, Solution of boundary value problems by integral equations of the first kind, *SIAM Rev.* **15**, 687 (1973).

13. A. Lyrintzis and Yu Xue, Versatile Kirchhoff code for aeroacoustic predictions, *AIAA J.* **35**, 198 (1997).

14. A. S. Lyrintzis and R. R. Mankbadi, Prediction of the far-field jet noise using Kirchhoff's formulation, *AIAA J.* **34**, 413 (1996).

15. K. R. Meadows and H. L. Atkins, Towards a highly accurate implementation of the Kirchhoff approach for computational aeroacoustics, *J. Comput. Acoust.* **4**, 225 (1996).

16. B. E. Mitchell, S. K. Lele, and P. Moin, Direct computation of the sound generated by vortex pairing in an axisymmetric jet, *J. Fluid Mech.* **383**, 113 (1999).

17. S. M. Patrick, *The Acoustic Directivity from Airfoils in Nonuniform Subsonic Flows*, M.S. dissertation (Univ. Notre Dame, Notre Dame, IN, 1993).

18. S. M. Patrick, C. M. Davis, and H. M. Atassi, *Acoustic Radiation from a Lifting Airfoil in Nonuniform Subsonic Flows*, FED-Vol. 147 (Computational Aero- and Hydro-Acoustics, ASME, 1993).

19. J. R. Scott, *Compressible Flows with Periodic Vortical Disturbances around Lifting Aiorfoils*, Ph.D. dissertation (Univ. Notre Dame, IN, 1990).

20. J. R. Scott and H. M. Atassi, A finite-difference, frequency-domain numerical scheme for the solution of the gust response problem, *J. Comput. Phys.* **119**, 75 (1995).

21. E. J. Stenger, *Calculating the Far-Field Acoustic Radiation from Airfoils Using Potential Theory*, M.S. thesis (Univ. Akron, Akron, OH, 1995).

22. S. Subramaniam, *Acoustic Radiation from Arbitrary Lifting Airfoils*, M.S. thesis (Dep. Aerosp. Mech. Eng., Univ. Notre Dame, Notre Dame, IN, 1990).

23. S. Subramanian, *Experimental and Computational Studies on Propeller Noise Due to Inflow Distortion*, Ph.D. dissertation (Univ. Notre Dame, Notre Dame, IN, 1993).

24. C. K. W. Tam, Advances in numerical boundary conditions for computational aeroacoustics, *J. Comput. Acoust.* **6**, 377 (1998).

25. C. K. W. Tam and J. C. Webb, Dispersion-relation-preserving schemes for computational acoustics, *J. Comput. Phys.* **107**, 262 (1993).